Journal of Statistical Physics, Vol. 107, Nos. 1/2, April 2002 (© 2002)

Preliminary Results in the Use of Energy-Dependent Octagonal Lattices for Thermal Lattice Boltzmann Simulations

Pavol Pavlo,[1] George Vahala,[2] and Linda Vahala[3]

Received February 19, 2000; accepted May 23, 2001

Thermal lattice Boltzmann simulations are prone to severe numerical instabilities. While octagonal velocity lattices increase the range of temperatures that can be successfully simulated, the ranges are insufficient for many applications. Second order interpolation is required to correlate diagonal streaming to the square spatial grid. Here, the role of energy-dependent octagonal lattices is examined, an idea spawned from Gauss–Hermite quadratures. A nontrivial allocation scheme is now required to ensure moment conservation in connecting to the spatial grid. For the energy-dependent lattices, it is shown that there are no lower bounds to the temperature, thus allowing for higher Reynolds number simulations. Simulations are presented and compared to theory (viscosity and sound speed dependence on temperature) showing excellent agreement.

KEY WORDS: Thermal lattice Boltzmann; octagonal lattices; simulations; jet turbulence.

1. INTRODUCTION

Lattice Boltzmann algorithms are an ideal mesoscopic approach to solving nonlinear macroscopic conservation equations because of their simplicity and ease of parallelization for multi-PE computers. In particular, lattice Boltzmann models (LBM) completely avoid the nonlinear Riemann problem that plague conventional computational fluid dynamics (CFD), and whose accurate resolution can take up over 30% of the total CPU.

[1] Institute of Plasma Physics, Czech Academy of Sciences, Prague 8, Czech Republic.
[2] Department of Physics, College of William & Mary, Williamsburg, Virginia 23187; e-mail: lgvahala@earthlink.net
[3] Department of Electrical & Computer Engineering, Old Dominion University, Norfolk, Virginia 23159.

0022-4715/02/0400-0499/0

LBM avoids the nonlinear Riemann problem by moving to kinetic phase space and solving the simple linear BGK kinetic equation

$$\frac{\partial f}{\partial t}+\xi\cdot\nabla f=-\frac{1}{\tau}[f-f^{eq}] \tag{1}$$

where f^{eq} is the relaxation (Maxwellian) distribution function

$$f^{eq}=\frac{n}{2\pi\varepsilon}\exp\left[-\frac{(\xi-\mathbf{u})^2}{2\varepsilon}\right] \tag{2}$$

n is the number density, u the mean velocity and ε is the temperature. τ controls the rate at which $f(\mathbf{x}, \xi, t)$ relaxes to f^{eq}. The nonlinear convective derivatives in CFD are now replaced by simple streaming in kinetic phase space. The price paid by LBM in avoiding the nonlinear Riemann problem is the increased dimensionality of phase space. For example, in two dimensional (2D) flows (and for simplicity we shall restrict all considerations to 2D flows), the phase space increases for 2 space + time → 2 space + 2 kinetic velocity + time. For fluid flows, particularly in the highly collisional regime, this seems a step backwards in solvability—an inverse statistical mechanical approach. However, what saves the day for LBM is the discretization algorithm in kinetic velocity space. Indeed, a minimal number of discrete velocities are chosen such that under Chapman–Enskog expansions, the discretized LBM reduces to the original nonlinear macroscopic conservation equations. The choice of lattice symmetry plays a vital role, not only in decreasing storage requirements but also in determining the range of values in $(n, \mathbf{u}, \varepsilon)$ for which one will achieve numerical stability.

Under discretization, the BGK kinetic equation (1), in LBM units, becomes

$$N_k(\mathbf{x}+\mathbf{c}_k, t+1)-N_k(\mathbf{x}, t)=-\frac{1}{\tau}[N_k(\mathbf{x}, t)-N_k^{eq}(\mathbf{x}, t)] \tag{3}$$

where $\mathbf{c}_k$ is the lattice velocity vector and the number of discrete velocities is b: $k=1,\ldots, b$. To stress the velocity discretization, we change our notation for the distribution function: $f(\mathbf{x}, \xi, t)\rightarrow N_k(\mathbf{x}, t)$. Because we have reduced the velocity phase space symmetry from continuous rotational symmetry to that of the discrete lattice, N_k cannot take the form of a discretized local Maxwellian. As a result, one no longer has an H-theorem and the positive-definiteness of N_k with time cannot be ensured. The achievable solution domain in $(n, \mathbf{u}, \varepsilon)$-space will thus be dependent on the choice of the lattice symmetry as well as on the form of N^{eq}.

For incompressible flows the LBM, Eq. (3) has achieved excellent success,[1–4] while straightforward models[5–12] employing closure at the energy moment level have struggled with numerical instabilities and the non-positive definiteness of N_k. There are two basic attempts that have been taken to combat this problem: (a) more general formulations[13–15] involving N_k^{eq}, or (b) introduce higher discrete isotropic lattices.[16, 17] In this paper, we continue with our exploration of using higher isotropy lattices—lattices which will no longer be space-filling.

In Section 2, we shall review the role of octagonal lattices in 2D (their 3D generalization has been presented in ref. 17), and then present the case for using energy-dependent octagonal lattices. Since this is new ground, we present some preliminary simulations for 2D jet flow between plane boundaries held at constant temperature. These results are presented in Section 4, with a brief summary in Section 5.

2. OCTAGONAL LATTICES

Most thermal LBM have worked with either the square or hexagonal velocity lattice, since these are space-filling and allow for the overlay of the velocity lattice onto the spatial grid. For thermal LBM, the mean variables are defined by the discretized moments of N_k^{eq}:

$$n(\mathbf{x}, t) = \sum_k N_k^{eq} \tag{4}$$

$$n(\mathbf{x}, t)\, \mathbf{u}(\mathbf{x}, t) = \sum_k N_k^{eq}\, \mathbf{c}_k \tag{5}$$

$$n(\mathbf{x}, t)\, \varepsilon(\mathbf{x}, t) + \tfrac{1}{2} n(\mathbf{x}, t)\, \mathbf{u}^2(\mathbf{x}, t) = \tfrac{1}{2} \sum_k N_k^{eq} \mathbf{c}_k^2 \tag{6}$$

with the relaxation distribution function having a series representation in powers of u/c_s, where c_s is the sound speed:

$$N_0^{eq} = n[A_0(\varepsilon) + C_0(\varepsilon)\, \mathbf{u}^2 + \cdots] \tag{7}$$

for the rest particles, and

$$N_k^{eq} = n[A_1(\varepsilon) + B_1(\varepsilon)(\mathbf{c}_k \cdot \mathbf{u}) + C_1(\varepsilon)\, \mathbf{u}^2 + D_1(\varepsilon)(\mathbf{c}_k \cdot \mathbf{u})^2 + \cdots] \tag{8}$$

for particles moving with velocity $\mathbf{c}_k$. The expansion coefficients $A_0, C_0, \ldots, A_1, \ldots$ are determined from (4)–(6) and to remove any discrete lattice effects that might appear in the long wavelength, long time Chapman–Enskog limit—equations which should be nothing but the nonlinear macroscopic conservation equations of interest.

It is important to note that the truncation error $O(u^p/c_s^p)$ in N_k^{eq} will determine the level of moments that can be satisfied in the closure scheme. For example, if the error terms are chosen to be of order u^4/c_s^4, then one will need to also satisfy the moment constraint (in component form)

$$\sum_k N_k^{eq} c_{k\alpha} c_{k\beta} c_{k\gamma} = n\varepsilon[u_\alpha \delta_{\beta\gamma} + u_\beta \delta_{\gamma\alpha} + u_\gamma \delta_{\alpha\beta}] + n u_\alpha u_\beta u_\gamma \tag{9}$$

This moment constraint is, of course, exactly satisfied in the continuum limit by the Maxwellian distribution.

The greater the level of isotropy of the chosen discrete velocity lattice, the less constraints are placed on the expansion coefficients in N_k^{eq} and the greater the range of values in $(n, \mathbf{u}, \varepsilon)$-space that can be achieved by a stable code. This can be readily seen by substituting Eqs. (7) and (8) into the moments Eqs. (4)–(6), (9),.... After this substitution, one needs to evaluate the nth-lattice vector moments:

$$T^n_{\alpha\cdots\xi} = \sum_k c_{k\alpha} \cdots c_{k\xi} \tag{10}$$

With 2D lattice vectors taking the form:

$$\mathbf{c}_k = (\cos)\, \mathbf{c}_k = \left(\cos \frac{\pi(k-1)}{K}, \sin \frac{\pi(k-1)}{K} \right) \tag{11}$$

where $k = 1,..., K$ with

square lattice: $K = 4$

hexagonal lattice: $K = 6$

octagonal lattice: $K = 8$

it can be readily shown that

$$T^4_{\alpha\beta\gamma\delta} = \psi \cdot \delta_{\alpha\beta\gamma\delta} + \phi \cdot (\delta_{\alpha\beta}\delta_{\gamma\delta} + \delta_{\alpha\gamma}\delta_{\beta\delta} + \delta_{\alpha\delta}\delta_{\beta\gamma}) \tag{12}$$

$$T^6_{\alpha\beta\gamma\delta\varepsilon\chi} = \Psi \cdot \delta_{\alpha\beta\gamma\delta\varepsilon\chi} + \Lambda \cdot (\delta_{\alpha\beta}\delta_{\gamma\delta\varepsilon\chi} + c \cdot p) + \Theta(\delta_{\alpha\beta} T^4_{\gamma\delta\varepsilon\chi} + c \cdot p) \tag{13}$$

where $\delta_{\ldots}$ is the Kronecker tensor, with $\delta_{\ldots} = 1$ if all the indices are equal and $\delta_{\ldots} = 0$ otherwise. Only the 2D tensor $\delta_{\alpha\beta}$ is isotropic. The coefficients $\psi, \phi, \Psi, \Lambda, \theta$ are dependent on the chosen lattice symmetry. Now for the square lattice $\psi \neq 0$, so that T^4 is not isotropic. For the hexagonal lattice $\psi = 0$, but $\Psi \neq 0$ so that the hexagonal symmetry leads to an isotropic T^4, but an anisotropic T^6. However, for the octagonal lattice $\psi = 0 = \Psi = \Lambda$ so that the octagonal symmetry results in the 6th rank lattice vector

moment T^6 being isotropic. Once the level of closure is chosen, the level of T^n-isotropy that is required is determined. Because of this requirement, if the chosen lattice symmetry will not in itself satisfy this isotropy (e.g., the square lattice), then the burden to ensure the required isotropy enforces constraints on the expansion coefficients. Thus the octagonal lattice should result in a more numerically stable algorithm.

Now for space-filling velocity lattices, in which the velocity lattice and spatial grid overlay each other, the usual algorithm for solving Eq. (3) is:

(i) free-stream $N_k(\mathbf{x}) \to N_k(\mathbf{x}+\mathbf{c}_k)$

(ii) recompute the mean variables $n, \mathbf{u}, \varepsilon$ by taking the appropriate moments of N_k and thus update the relaxation distribution $N_k^{eq} = N_k^{eq}(n; \mathbf{u}; \varepsilon)$,

(iii) collisional relaxation at each spatial grid node

$$N_k(\mathbf{x}) - \frac{1}{\tau}[N_k(\mathbf{x}) - N_k^{eq}(\mathbf{x})] \to N_k(\mathbf{x}) \qquad \text{at time} \quad t+1$$

Let us now consider the choice of the non-space filling octagonal velocity lattice.[16] It is convenient to take a square spatial grid. However for the octagonal lattice the streaming in the diagonal directions results in spatial positions $\mathbf{x}+\mathbf{c}_k$, $k = 2, 4, 6, 8$ which do not coincide with the square grid nodes. As a result, we must introduce a further step in the LBM algorithm:

(i′) second order interpolation in the diagonal directions.

The improvement in numerical stability of the higher isotropy octagonal lattice can be immediately seen in Table I, in which we present the stable temperature range at a relaxation decay rate $\tau = 0.504$.

While the results[16, 17] for an octagonal lattice are encouraging, the allowed stable solution range in $(n, \mathbf{u}, \varepsilon)$-space is still too restrictive for application to turbulence problems in the tokamak divertor region,

Table I. Parameter Regime in Temperature for Stable LBM at $\tau = 0.504$. There Are No Stable Temperature Range for Square Lattices, While for Hexagonal Lattices There Are Two Very Narrow Disjoint Intervals. However, for Octogonal Lattices, There Is a Continuous and Wide Stable Energy Range

$\tau = 0.504$	Square	Hexagonal	Octogonal
Stability limits on the temperature ε	–	$0.32 < \varepsilon < 0.35$ $0.49 < \varepsilon < 0.505$	$0.28 < \varepsilon < 0.555$

a problem of considerable interest to us.[18–20] This has driven us to consider energy-dependent octagonal lattices.

3. ENERGY-DEPENDENT OCTAGONAL LATTICES

The role of energy-dependent lattices becomes evident when extending the Gaussian–Hermite quadrature technique from momentum closure[21] to energy closure schemes.[17] The Gauss–Hermite method allows for the determination of both the relaxation distribution function as well as the velocity lattice itself. We now briefly review this approach. In the continuum velocity phase space, the relaxation distribution f^{eq} in the BGK kinetic equation (1), is the Maxwellian (in 2D):

$$f^{eq} = \frac{n}{2\pi\varepsilon} \exp\left[-\frac{(\xi - \mathbf{u})^2}{2\varepsilon} \right] \tag{14}$$

Suppose a minimal Taylor expansion in the mean velocity is performed on (14):

$$f^{eq} \approx \frac{n}{2\pi\varepsilon} \exp\left[-\frac{\xi^2}{2\varepsilon} \right] \left\{ 1 + \frac{\xi \cdot \mathbf{u}}{\varepsilon} - \frac{\mathbf{u}^2}{2\varepsilon} + \frac{(\xi \cdot \mathbf{u})^2}{2\varepsilon^2} - \frac{(\xi \cdot \mathbf{u})\,\mathbf{u}^2}{2\varepsilon^2} + \frac{(\xi \cdot \mathbf{u})^3}{6\varepsilon^3} + O(u^4) \right\} \tag{15}$$

The moments n, $n\mathbf{u}$, $n\varepsilon$ will be conserved if one can exactly evaluate the moment integrals up to second order (in Cartesian coordinates)

$$\int d^2\xi \, f^{eq} \xi_x^p \xi_y^q \qquad \text{for} \quad p+q \leqslant 2 \tag{16}$$

i.e., if one can exactly evaluate

$$\int_{-\infty}^{\infty} d\zeta \, \zeta^m \exp[-\zeta^2], \quad m \leqslant 5 \qquad \text{with} \quad \xi_{x,y} \equiv (2\varepsilon)^{1/2} \zeta \tag{17}$$

For a given M, Gaussian–Hermite quadratures yield the following integral estimate

$$\int_{-\infty}^{\infty} d\zeta \, h(\zeta) \exp[-\zeta^2] = \sum_{p=1}^{M} \omega_p h(\zeta_p) + O(h^{(2M)}(\zeta_*)) \tag{18}$$

where $h(\zeta)$ is an arbitrary function, and the error term is dependent on the $2M$th derivative of $h(\zeta)$. ζ_p are the zeros of the Hermite polynomial H_M, with $p = 1,..., M$

$$H_M(\zeta_p) = 0, \qquad p = 1,..., M \tag{19}$$

while the weight factor ω_p

$$\omega_p = \frac{2^{M+1} M! \sqrt{\pi}}{[H_{M+1}(\zeta_p)]^2}, \qquad p = 1,..., M \tag{20}$$

Hence we will have an exact representation for (17) for the choice $M = 3$, with nodal positions

$$\xi_1 = 0, \qquad \xi_2 = \sqrt{3\varepsilon}, \qquad \xi_3 = -\sqrt{3\varepsilon} \tag{21}$$

The corresponding phase space velocity lattice vectors are thus (in Cartesian coordinates)

$$\mathbf{c}_{ij} \equiv (\xi_i, \xi_j) = \mathbf{c}_{ij}(\varepsilon), \qquad i, j = 1, 2, 3 \tag{22}$$

i.e., the 9-bit velocity lattice vectors form a temperature-dependent square lattice.

We now report on some preliminary results using a 9-bit, 2D energy-dependent octagonal lattice representation of the linear BGK kinetic equation. We have chosen to work with the octagonal lattice rather than the square lattice since octagonal lattice symmetries have much better numerical stability[16] than that of the square (see also Table I). In this current paper, we do not fully exploit this T^6 isotropy of the octagonal lattice that will permit the accurate representation of the 6th moment integrals in Eq. (18). This would require multiple level of speeds (this is currently under investigation and will be reported elsewhere). We introduce the lattice vectors

$$\mathbf{c}_0 = 0; \qquad \mathbf{c}_k = c(\varepsilon)\, \mathbf{e}_k, \quad k = 1,..., 8 \tag{23}$$

where $\mathbf{e}_k$ is an octagonal unit vector:

$$\mathbf{e}_k = \left(\cos \frac{\pi(k-1)}{8}, \sin \frac{\pi(k-1)}{8} \right), \qquad k = 1,..., 8 \tag{24}$$

and $c(\varepsilon)$ is a scaling temperature-dependent parameter to be determined later.

The equilibrium distribution function is assumed to have the form

$$\begin{aligned} N_0^{eq} &= n(A_0(\varepsilon) + C_0(\varepsilon)\,\mathbf{u}^2) \\ N_k^{eq} &= n[A_1(\varepsilon) + B_1(\varepsilon)(\mathbf{c}_k \cdot \mathbf{u}) + C_1(\varepsilon)\,\mathbf{u}^2 + D_1(\varepsilon)(\mathbf{c}_k \cdot \mathbf{u})^2], \quad k = 1,\ldots, 8 \end{aligned} \tag{25}$$

for appropriately chosen coefficients $A_0(\varepsilon),\ldots, D_1(\varepsilon)$. On substituting Eq. (25) into the definition of the mean density, mean velocity and internal energy

$$\begin{aligned} n(\mathbf{x}, t) &= \sum_{k=0}^{8} N_k^{eq}, \quad n(\mathbf{x}, t)\,\mathbf{u}(\mathbf{x}, t) = \sum_{k=1}^{8} \mathbf{c}_k N_k^{eq}, \\ 2n(\mathbf{x}, t)\,\varepsilon(\mathbf{x}, t) &= \sum_{k=1}^{8} \mathbf{c}_k^2 N_k^{eq} - n\mathbf{u}^2 \end{aligned} \tag{26}$$

the octagonal symmetry constraints yield the following unique set of temperature-dependent coefficients

$$\begin{aligned} A_0 &= \frac{1}{2}, \quad C_0 = -\frac{1}{c^2(\varepsilon)}, \\ A_1 &= \frac{1}{16}, \quad B_1(\varepsilon) = \frac{1}{4c^2(\varepsilon)}, \quad C_1(\varepsilon) = -\frac{1}{8c^2(\varepsilon)}, \quad D_1(\varepsilon) = \frac{1}{2c^4(\varepsilon)} \end{aligned} \tag{27}$$

and the temperature-dependent scaling factor

$$c(\varepsilon) = \sqrt{4\varepsilon} \tag{28}$$

3.1. Implementation of the Energy-Dependent Algorithm

As usual, the lattice Boltzmann equation (3) is solved by splitting the algorithm into free streaming and collisional relaxation at each spatial node. However, now the free streaming is dependent on the temperature at that particular spatial node, with the streaming distance $|\mathbf{c}_k| = c(\varepsilon)$ varying from spatial node to spatial node since $\varepsilon = \varepsilon(\mathbf{x}, t)$. Of course, at each spatial node the octagonal phase space symmetry is preserved ($k = 1,\ldots, 8$).

3.1.1. Free Streaming

In general, after the distributions N_k are streamed in the direction $\mathbf{e}_k$ ($k = 1,\ldots, 8$) by the distance $c(\varepsilon)$, their spatial locations will no longer coincide with the spatial grid nodes. Moreover these spatial locations will, throughout the spatial domain, be non-equidistant from the spatial grid nodes because of the spatial dependence of the temperature. It is not

straightforward to design an interpolation scheme that will conserve the macroscopic moments (26) and yield the distributed values of the N_k's onto the given spatial grid. This is particularly true since the various off-grid streamed N_k's will have come from spatial nodes at different temperature. This would then require further interpolations for the moments $\sum N_k \mathbf{c}_k$ and $\sum N_k \mathbf{c}_k^2$ with the strong likelihood of introduction significant numerical viscosity.

Instead, we utilize an allocation algorithm for determining how some function $F(\mathbf{x}+\mathbf{c}_k)$, following streaming, is to be distributed among the neighboring spatial grid nodes $\mathbf{x}+\ell\mathbf{e}_k$, for some integer ℓ. Although we work here with the standard 2D square grid, this allocation scheme can be readily extended to any non-uniform spatial grid.

Let Λ_ℓ be the fraction of $F(\mathbf{x}+\mathbf{c}_k)$ that is to be allocated to the spatial node $\mathbf{x}+\ell\mathbf{e}_k$ for a given k. Normalizing over all the allocations,

$$\sum_\ell \Lambda_\ell = 1 \tag{29}$$

Further, by allocating a portion Λ_ℓ of $F(\mathbf{x}+\mathbf{c}_k)$ to the nodes $\mathbf{x}+\ell\mathbf{e}_k$, we can, in fact, consider that one has streamed to the spatial node itself $\mathbf{x}+\ell\mathbf{e}_k$, rather than to $\mathbf{x}+c\mathbf{e}_k$. However, to recover proper convection, one must impose the constraints on the allocation factors Λ_ℓ:

$$n\mathbf{u} = \sum_k N_k c\mathbf{e}_k = \sum_k N_k \sum_\ell \Lambda_\ell \ell \mathbf{e}_k \tag{30}$$

and

$$n\varepsilon + \tfrac{1}{2} n\mathbf{u}^2 = \tfrac{1}{2}\sum_k N_k c^2 = \tfrac{1}{2}\sum_k N_k \sum_\ell \Lambda_\ell \ell^2 \tag{31}$$

Thus, the allocation factors must satisfy

$$\sum_\ell \Lambda_\ell \ell = c(\varepsilon), \qquad \sum_\ell \Lambda_\ell \ell^2 = c^2(\varepsilon), \qquad \sum_\ell \Lambda_\ell = 1 \tag{32}$$

Two possible stencils that satisfy (32) are:

$$\begin{aligned} &\#1: \quad \ell = (-1, 0, 1) \quad \text{with} \quad \Lambda_{-1} = \tfrac{1}{2}(\alpha^2 - \alpha), \\ &\Lambda_1 = \tfrac{1}{2}(\alpha^2 + \alpha) \quad \text{and} \quad \Lambda_0 = 1 - \Lambda_{-1} - \Lambda_1 \end{aligned} \tag{33}$$

$$\begin{aligned} &\#2: \quad \ell = 0, 1, 2 \quad \text{with} \quad \Lambda_1 = 2\alpha - \alpha^2, \\ &\Lambda_2 = \tfrac{1}{2}(\alpha^2 - \alpha) \quad \text{and} \quad \Lambda_0 = 1 - \Lambda_1 - \Lambda_2 \end{aligned} \tag{34}$$

where

$$\alpha = c(\varepsilon) \text{ for } k \text{ odd (i.e., for streaming along the axes)}$$
$$\alpha = \frac{c(\varepsilon)}{\sqrt{2}}, \text{ for } k \text{ even (i.e., for streaming along the diagonals)} \tag{35}$$

Contributions to a particular spatial grid node will come from several nearby nodes corresponding to different temperatures, i.e., different $c(\varepsilon)$. Therefore, to ensure an exact conservation of the macroscopic moments, not only must one stream the distributions N_k but also the corresponding parts of the momentum and energy carried by the individual distributions, i.e., one must also stream $N_k\alpha$ and $N_k\alpha^2$. These must be saved in arrays for $\mathbf{u}$ and ε so that the integration step is combined with the streaming.

3.1.2. Collision

From (3), the typical collision routine in lattice Boltzmann simulations would be

$$\left(1-\frac{1}{\tau}\right)N_k(t)+\frac{1}{\tau}N_k^{eq}(t) \rightarrow N_k(t+1) \tag{36}$$

in order to obtain the distribution function from time $t \rightarrow t+1$. However the situation is a bit more complex for energy-dependent lattices. Since $c = c(\varepsilon)$ is dependent on the particular spatial grid, (36) is replaced by

$$\left(1-\frac{1}{\tau}\right)\overline{N_k(t)}+\frac{1}{\tau}N_k^{eq}(t) \rightarrow N_k(t+1) \tag{37}$$

where the distributions $\overline{N_k(t)}$ are the distributions $N_k(t)$ (before collision), but renormalized to account for the new velocity lattice [because of the new $c(\varepsilon)$] used in determining N_k^{eq}, since the streaming step has been performed first. Thus, $\overline{N_k(t)}$ are renormalized to satisfy the moment constraints

$$\sum_k \overline{N_k} = n, \qquad \sum_k \overline{N_k} c(\varepsilon)\, \mathbf{e}_k = n\mathbf{u}, \qquad \sum_k \overline{N_k} c^2(\varepsilon) = 2n\varepsilon + n\mathbf{u}^2 \tag{38}$$

for the new values of n, $\mathbf{u}$, $c(\varepsilon)$.

4. 2D JET FLOW SIMULATIONS BETWEEN WALLS HELD AT CONSTANT TEMPERATURE

Before presenting results for 2D jet flow between constant temperature walls, we first consider a numerical test of the energy-dependent lattice

algorithm. We shall determine the temperature dependence of the viscosity for plane Poiseuille flow and compare it to the theoretical (Chapman–Enskog) result:

$$\nu_{\text{theor}} = \varepsilon(\tau - \tfrac{1}{2}) \tag{39}$$

which is, of course, independent of the channel width. For the simulations, we introduce a forcing term **f** on the left hand side of Eq. (2). For simple Poiseuille flow, it is well known that the viscosity is related to the momentum at the channel center

$$\nu = \frac{L^2}{8u_0} f \tag{40}$$

where u_0 is velocity at the channel center and L is the channel width. For a given channel width and forcing, we determine the mean velocity at the channel center from the simulations and hence the viscosity by Eq. (40). These simulation results are shown in Figs. 1(a) and (b) for the allocation scheme #1 and scheme #2. The open circles are the simulation results for a channel width $L = N_y = 32$, while the filled square are for a channel width $L = N_y = 80$. The full line, dashed line.... are the theoretical results from Eq. (39). One finds very good agreement between theory and simulation over a very wide range of temperatures. It is evident that there is some deviation of our simulation results from theory for channel width $L = N_y = 32$—particularly as $\tau \to 0.5_+$ for temperatures $\varepsilon < 10^{-2}$. Since our algorithm no longer runs at a kinetic CFL = 1, it is important to determine if these deviations are induced by numerical viscosity introduced by our streaming allocation algorithm. To test this, we have increased the channel width to $L = N_y = 80$ and the results are shown as filled squares in Figs. 1(a) and (b). We find excellent agreement between theory and simulation: e.g., for allocation scheme #1, with $\varepsilon = 5 \times 10^{-2}$ and $\tau = 0.52$, Eq. (39) yields $\nu_{\text{theor}} = 1.0000 \times 10^{-4}$ while our simulation results Eq. (40) yield $\nu = 1.0025 \times 10^{-4}$. We thus conclude that the deviations for temperatures $\varepsilon < 10^{-2}$ and small τ are a consequence of channel width size and not numerical viscosity. This can be seen further in Fig. 1c where the effects of channel width on the viscosity are plotted as a function of the number of iterations performed to reach the steady state Poiseuille flow for allocation scheme #2 for $\tau = 0.6$, $\varepsilon = 5 \times 10^{-3}$. For channel widths $L = N_y = 80$, one attains excellent agreement with the theoretical viscosity, albeit at the price of the number of iterations.

From the point of view of numerical stability, we find there is an upper bound on the internal energy ε, which depends on the particular

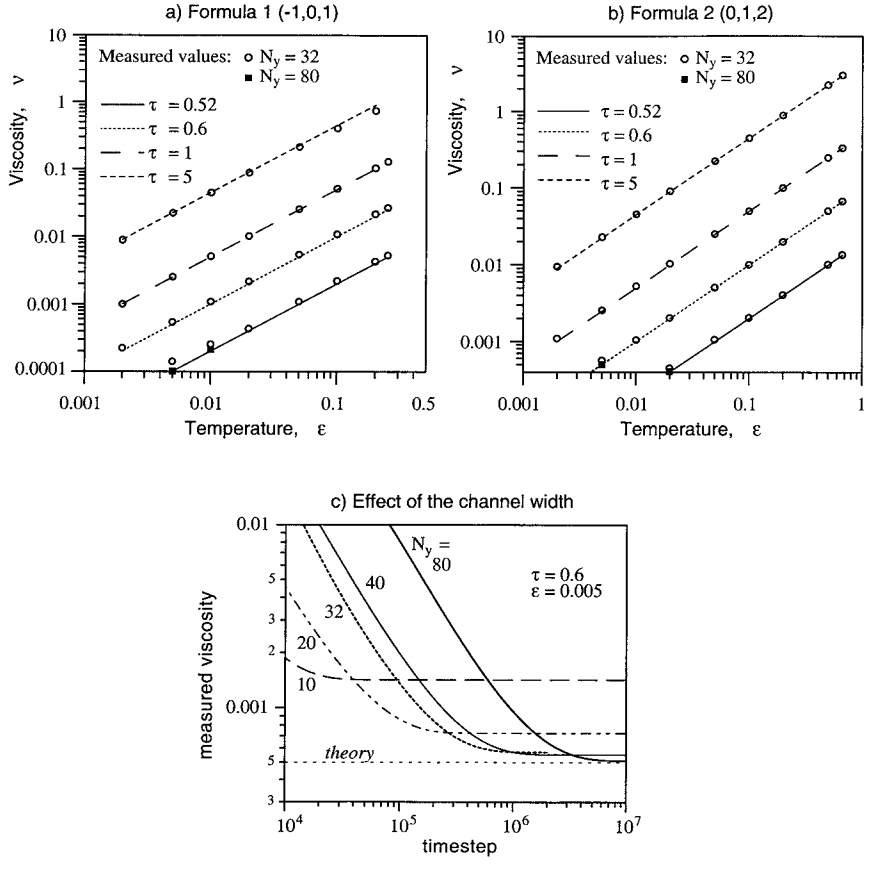

Fig. 1. A comparison of theoretical (from Chapman–Enskog) and simulation (from Poiseuille flow) determinations for the viscosity transport coefficient for 2 different allocation schemes: (a) allocation scheme $\ell = -1, 0, 1$, and (b) allocation scheme $\ell = 0, 1, 2$. The open dots are the lattice Boltzmann energy-dependent octagonal lattice simulation results for channel width $N_y = 32$, while the filled squares are for channel width $N_y = 80$. The lines are the theoretical results for different values of relaxation rates τ. (c) plots the effect of channel width N_y on the simulation viscosity as a function of the number of time iterations.

streaming allocation scheme chosen: for allocation scheme #1 $\varepsilon \leqslant 0.25$, while for allocation scheme #2 $\varepsilon \leqslant 0.67$. However, it is critical to note that there are no lower bounds on ε. Thus one can achieve quite high Reynolds

$$\mathrm{Re} = \frac{V_0 L}{\nu} = \frac{V_0 L}{\varepsilon(\tau - 0.5)} \tag{41}$$

simply by letting $\varepsilon \to 0$, where V_0 is a typical velocity and L is a typical length. This should be contrasted with the results achieved from fixed octagonal lattice vectors, Table I, where the lower bound on ε is solidly bounded away from zero. Finally, the linear stability of the energy-dependent octagonal lattice (for either allocation scheme) places an upper bound on the Mach number

$$\mathrm{Ma} = \frac{V_0}{c_s} \leqslant 0.5 \tag{42}$$

where c_s is the sound speed.

4.1. Scaling of Sound Speed with Temperature

Theoretically, the sound speed

$$c_s = \sqrt{2\varepsilon} \tag{43}$$

To test the energy-dependent lattice concept we perform a series of jet simulation at fixed Reynolds number $\mathrm{Re} = 2{,}500$ and Mach number $\mathrm{Ma} = 0.5$. We vary the values of the temperature from $\varepsilon = 0.5$ to $\varepsilon = 8 \times 10^{-6}$ and adjust the other parameters in (42) and (43) accordingly so that Re and Ma remain invariant (see Table II).

The simulation grid chosen was 200×40, the nozzle width was $L = 5$ and the nozzle protrusion in the horizontal direction was 14 lattice units. The time output of the density profiles, t_{out}, is chosen in the 4 runs so that $(2\varepsilon)^{1/2} \times t_{\mathrm{out}}$ is the same in all the cases. From the density plots in Fig. 2(a)–(d), one can ascertain the leading edge of the wave front for these parameters and there is very good agreement between all 4 runs that indeed $c_s = \sqrt{2\varepsilon}$ holds. It should be noted that as ε is chosen smaller and smaller, the corresponding V_0 must also decrease because of the stability limit on

Table II. Parameter ε, V_0, τ for 4 Different Runs (a)–(b) at the Same Reynolds and Mach Numbers. The Time Output, t_{out}, Is Choosen in These Runs so that $(2\varepsilon)^{1/2} t_{\mathrm{out}} = \mathrm{const}$.

	(a)	(b)	(c)	(d)
ε	0.5	0.02	2×10^{-4}	8×10^{-6}
V_0	0.5	0.1	0.01	0.002
τ	0.502	0.51	0.6	1.0
t_{out}	120	600	6,000	30,000
$(2\varepsilon)^{1/2} t_{\mathrm{out}}$	120	120	120	120

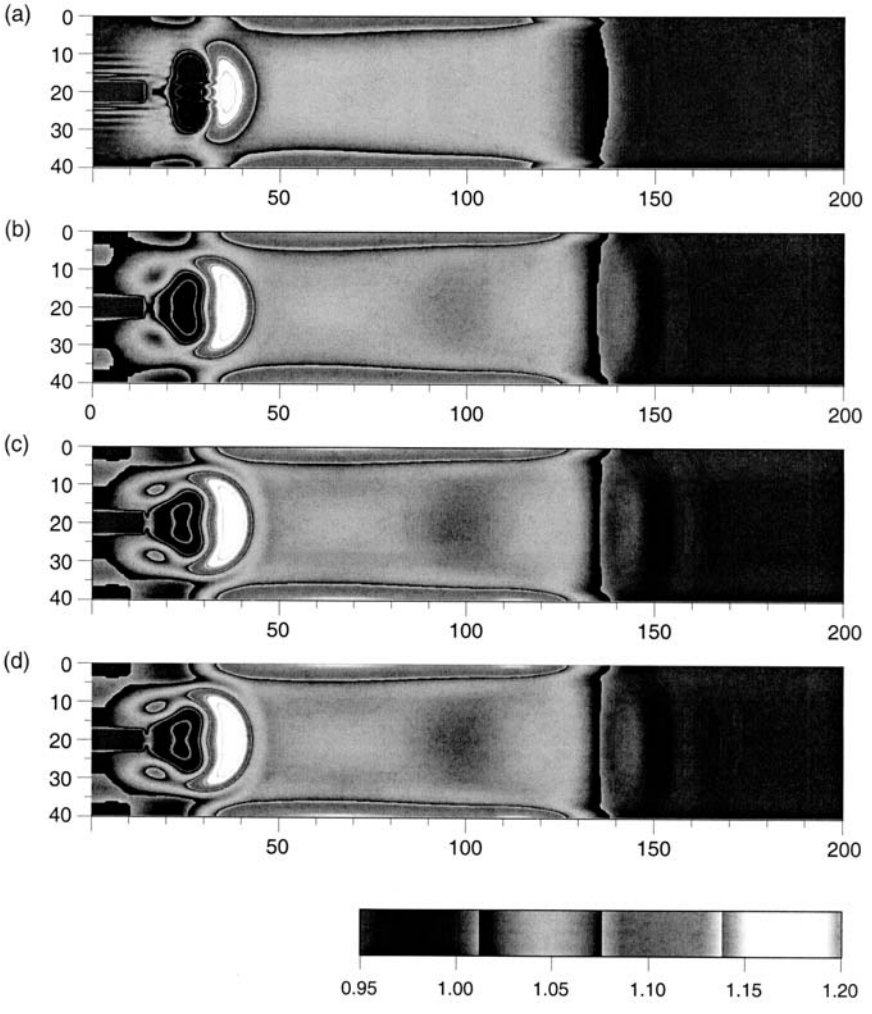

Fig. 2. Density profiles illustrating the scaling of the sound speed with temperature. The energy-dependent lattice algorithm is tested to verify the theoretical scaling $c_s = \sqrt{2\varepsilon}$ for energy values (a) $\varepsilon = 0.5$, (b) $\varepsilon = 0.02$, (c) $\varepsilon = 2 \times 10^{-4}$, and (d) $\varepsilon = 8 \times 10^{-6}$. The parameters are varied such that the four simulation are performed at the same Reynolds number and the same Mach number. The output time for these simulations is so chosen that $\varepsilon^{1/2} t_{\text{out}} = const.$ so that the wave front of the sound wave should be at the same spatial location for (a)–(d). The simulations bear out this sound speed scaling with temperature.

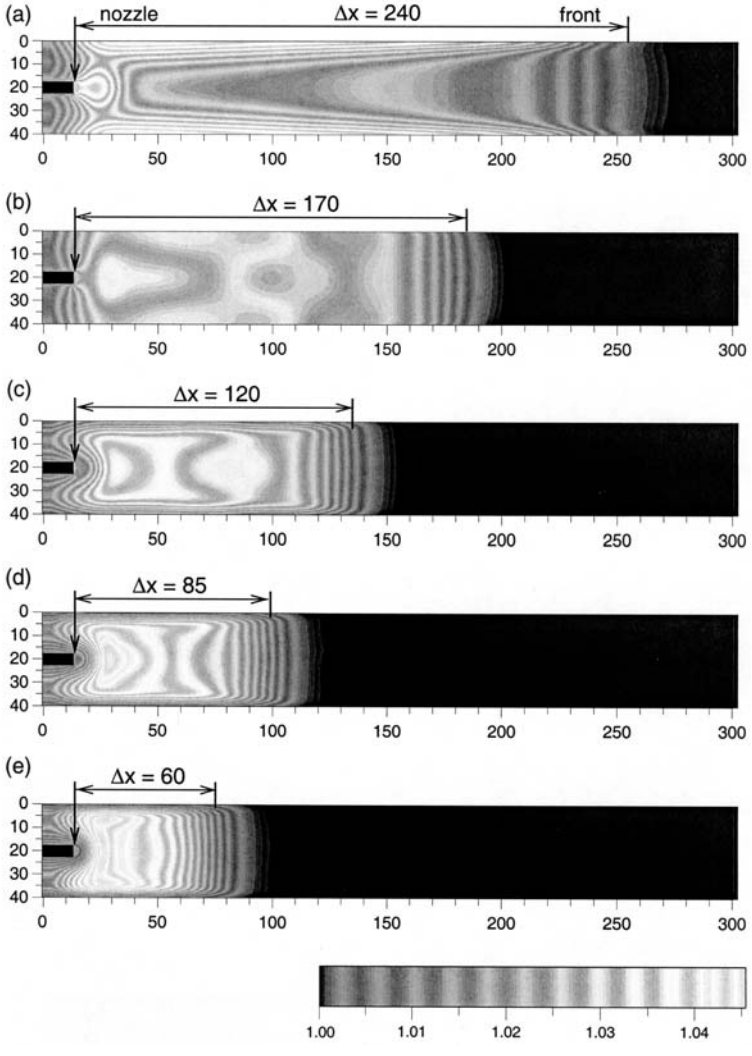

Fig. 3. Density profiles verifying the existence of an energy streaming factor C_ε. For relaxation rates $\tau = 1$ and temperature $\varepsilon = 0.18$ and after 400 time iterations, the density is shown for 5 different values of C_ε (see Table III). The theoretical location of the wave front is illustrated on these plots by the value of Δx. Again, one find excellent agreement between theory and simulation.

Table III. The Position of the Wave Front After 400 Iterations for Various Energy Scaling Parameter Values C_ε

C_ε	$\Delta x = c_s \cdot t_0 = t_0 \sqrt{C_\varepsilon 2\varepsilon}$
0.0625	60
0.125	84.85
0.25	120
0.5	169.7
1.0	240

the Mach number, (42). As a result, the number of lattice Boltzmann time iterations must be increased to get to the same stage of evolution.

4.2. Propagation of Wave Front at t_0=400

Another feature of our energy-dependent lattice is the freedom of introducing a streaming scaling factor C_ε for the energy. Theoretically, the sound speed now rescales to

$$c_s = \sqrt{C_\varepsilon \cdot 2\varepsilon} \tag{44}$$

Equation (44) is tested for various choices of the energy streaming factor C_ε at $\tau = 1$ and $\varepsilon = 0.18$. The density is shown in Fig. 3 at the same time output $t_0 = 400$ for 5 different values of C_ε. The theoretical wavefront position

$$\Delta x = c_s \cdot t_0 = t_0 \sqrt{C_\varepsilon 2\varepsilon} \tag{45}$$

is tabulated in Table III and compared to the simulation results in Fig. 3(a)–(e). Again, very good agreement is found between theory and simulation.

Table IV. The Parameters to Test the Integrity of Turbulence Simulations as $\varepsilon \to 0$ for Energy-Dependent Lattices

(a): $\sqrt{2\varepsilon_0} \cdot t_0 = 1200$	(b): $\sqrt{2\varepsilon_1} \cdot t_1 = 1200$
$V_0 = 0.002$	$V_1 = 0.01$
$t_0 = 300$ K	$t_1 = 60$ K
$\varepsilon_0 = 8 \times 10^{-6}$	$\varepsilon_1 = 2 \times 10^{-4}$
$\tau_0 = 1.0$	$\tau_1 = 0.6$

4.3. Integrity of Energy-Dependent Lattices for Given Reynolds Number and Mach Number

Finally, we consider a snapshot of jet turbulence between isothermal walls for the two parameter sets of values given in Table IV.
For this choice of parameters, the Reynolds numbers are equal

$$(\mathrm{Re})_0 = \frac{V_0 L}{\varepsilon_0(\tau_0 - 0.5)} = (\mathrm{Re})_1 = \frac{V_1 L}{\varepsilon_1(\tau_1 - 0.5)} = 2{,}500$$

as are the Mach numbers (the energy scaling factor here being unity, $C_\varepsilon = 1$)

$$(\mathrm{Ma})_0 = (\mathrm{Ma})_1 = 0.5$$

For a time snapshot with the equivalent physics in these two runs, we must choose these times t_0 and t_1 such that

$$\frac{t_0}{t_1} = \left(\frac{\varepsilon_1}{\varepsilon_0}\right)^{1/2} \tag{46}$$

Using a spatial grid of 200×40, the corresponding density profiles are shown in Fig. 4A. The upper figure is for case (a) after 300 K iterations, while the lower figure is for case (b) after 60 K iterations. The corresponding temperature profiles are shown in Fig. 4B and the axial jet velocity in Fig. 4C. Finally, we show the corresponding vorticity contours in Fig. 4D. Excellent agreement is found in all cases.

5. SUMMARY AND CONCLUSION

Conventional thermal lattice Boltzmann simulations using the linear BGK collision term are restricted to very narrow regions in $(n, \mathbf{u}, \varepsilon)$-space due to numerical instabilities. One can attempt to increase the solution-space domain by either concentrating on the form of N^{eq} (e.g., entropic approaches,...) or by considering higher order (discrete) symmetry lattices. Our research has centered on using higher order symmetry lattices, both in 2D and 3D. In particular, in 2D, we have concentrated on the octagonal lattice for the kinetic phase space velocity. Since these higher symmetry lattices are no longer space-filling, one must introduce some scheme to correlate the velocity lattice to the spatial grid. For octagonal lattices, a second order interpolation scheme in the diagonal directions is appropriate for a square spatial grid. Moreover, the introduction of this second order interpolation scheme does not introduce errors into the transport

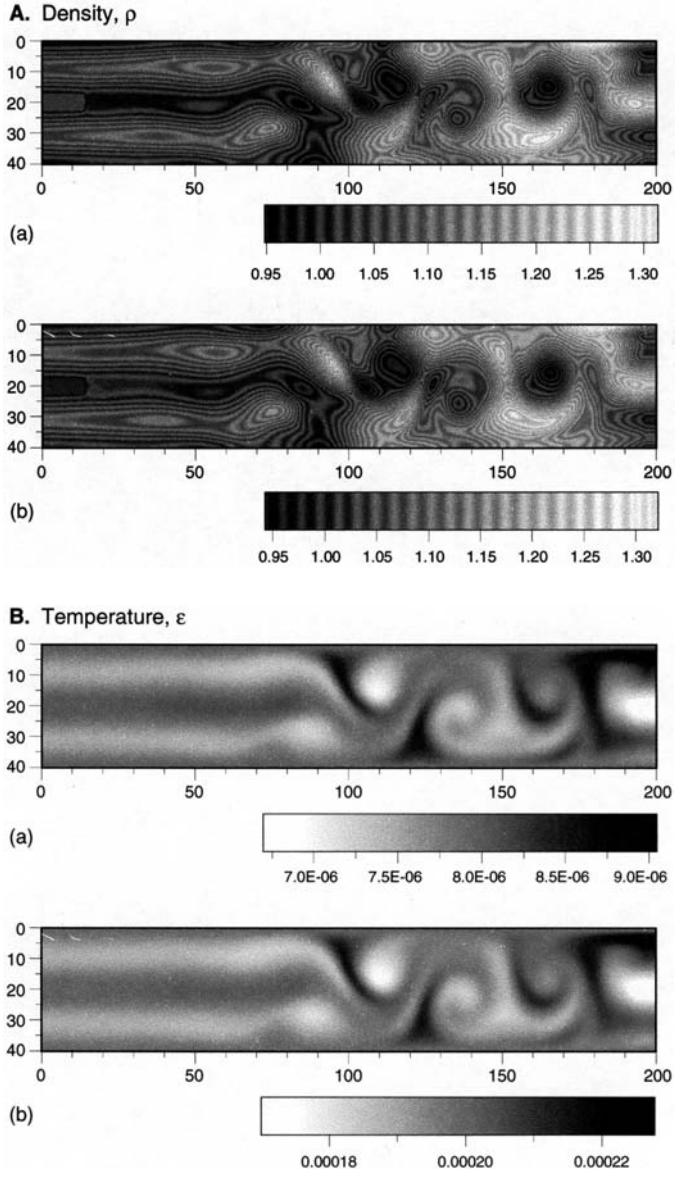

Fig. 4. Testing the integrity of energy-dependent octagonal lattices at Re = 2500, Ma = 0.5. For the parameters chosen (see Table IV), the simulation results for (a) and (b) should present the same physics: (A) density profile, (B) temperature profile, (C) axial velocity vx, and (D) vorticity contours. Excellent agreement is found.

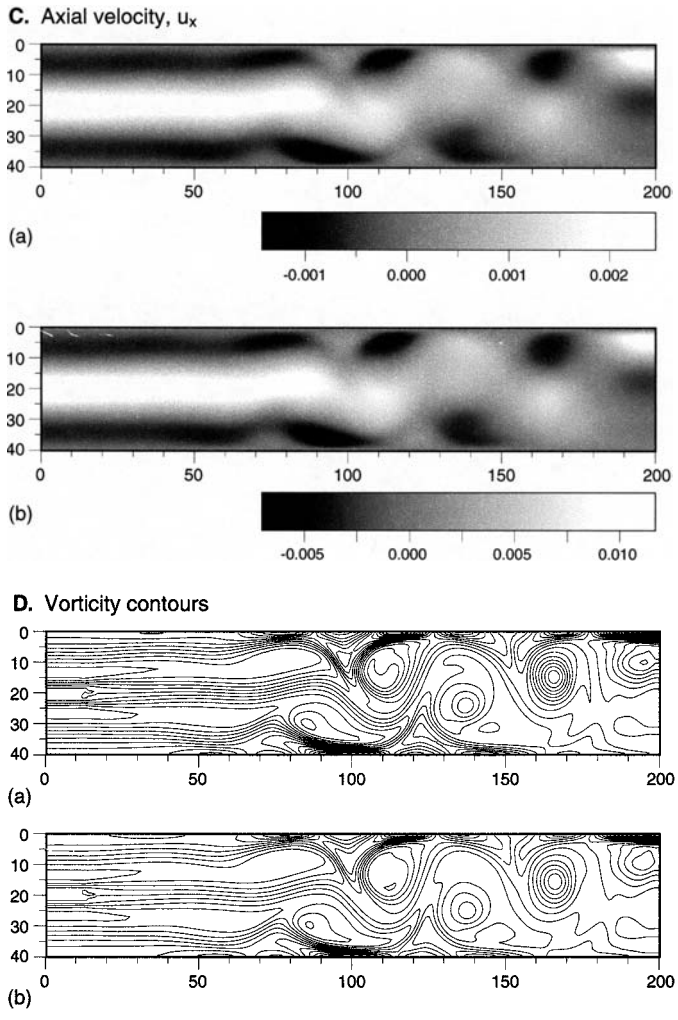

Fig. 4. (Continued).

coefficients. While the octagonal lattice substantially increases the solution domain in (n, $\mathbf{u}$, ε)-space, it is still not sufficient for certain application of interest to us—in particular, in application to the tokamak plasma divertor region.

On applying the Gauss–Hermite quadrature method to thermal flows, the associated velocity lattice now becomes temperature dependent. We have thus introduced here an energy-dependent octagonal 2D velocity lattice. Because the streaming operation in solving the discrete lattice Boltzmann equation is now temperature-dependent, a non-trivial allocation scheme

must be introduced that will enforce the appropriate moments. Because the constraints to be enforced are quite complex, appropriate interpolation schemes are extremely hard to find. To test the allocation scheme considered here, we have thus restricted our analysis to the 9-bit model, a restricted model that does not solve the full non-linear energy equation.

One of the consequences of the energy-dependent octagonal lattice, as opposed to conventional lattices (and even the octagonal lattice), is that there is now no lower bound to the temperature: $\varepsilon \to 0$. This allows for quite high Reynolds number simulations by simply letting $\varepsilon \to 0$. Even at temperatures $\tau = 5 \times 10^{-3}$ and small τ, we do not see any effects of numerical viscosity being introduced by our allocation scheme. A drawback to using very small ε, however, is the increased number of time iterations (since the Mach number cannot exceed 0.5 for a numerically stable code).

The energy-dependent lattice simulations of Poiseuille flow yielded the viscosity dependence on temperature in excellent agreement with theory. Moreover, our simulations showed excellent dependence of sound speed on temperature as well as the integrity of scaling with different parameters at the same Reynolds number and Mach number.

Because of the success of our 9-bit model as reported here, we are now working on the full 17-bit model. The results of this will be reported elsewhere.

ACKNOWLEDGMENTS

This work was supported by the Czech Academy (P.P.) GACR 202/00/1216 and DoE (G.V., L.V.).

REFERENCES

1. U. Frisch, D. d'Humieres, B. Hasslacher, P. Lallemand, Y. Pomeau, and J.-P. Rivet, *Complex Syst.* **1**:649 (1987).
2. S. Wolfram, *J. Stat. Phys.* **45**:471 (1986).
3. R. Benzi, S. Succi, and M. Vergassola, *Phys. Rep.* **222**:145 (1992).
4. S. Chen an G. D. Doolen, *Annu. Rev. Fluid Mech.* **30**:329 (1998).
5. F. J. Alexander, S. Chen, and J. D. Sterling, *Phys. Rev. E* **47**:2249 (1993).
6. Y. Chen, H. Ohashi, and M. Akiyama, *Phys. Rev. E* **50**:2276 (1994).
7. G. McNamara and B. J. Alder, *Physica A* **194**:218 (1993).
8. G. T. McNamara, A. L. Garcia, and B. J. Alder, *J. Stat. Phys.* **81**:395 (1995).
9. P. Pavlo, G. Vahala, L. Vahala, and M. Soe, *J. Comput. Phys.* **139**:79 (1998).
10. M. Soe, G. Vahala, P. Pavlo, L. Vahala, and H. Chen, *Phys. Rev. E* **57**:4227 (1998).
11. L. Vahala, D. Wah, G. Vahala, J. Carter, and P. Pavlo, *Phys. Rev. E* **62**:407 (2000).
12. G. Vahala, J. Carter, D. Wah, L. Vahala, and P. Pavlo, in *Parallel Computational Fluid Dynamics*, D. Keyes, A. Ecer, N. Satofuka, P. Fox, and J. Periaux, eds. (North-Holland, Amsterdam, 2000), pp. 423–431.

13. A. Renda, G. Bella, S. Succi, and I. V. Karlin, *Europhys. Lett.* **41**:279 (1998).
14. I. V. Karlin, A. Ferrante, and H. C. Ottinger, *Europhys. Lett.* **47**:182 (1999).
15. B. M. Boghosian, J. Yepez, P. V. Coveney, and A. Wagner, *Proc. Roy. Soc.* (to be published).
16. P. Pavlo, G. Vahala, and L. Vahala, *Phys. Rev. Lett.* **80**:3960 (1998).
17. G. Vahala, P. Pavlo, L. Vahala, and N. S. Martys, *Internat. J. Modern Phys. C* **9**:1247 (1998).
18. R. Janneschitz, *J. Nucl. Mater.* **220–222**:67 (1995).
19. D. Knoll, P. R. McHugh, S. I. Krasheninnikov, and D. J. Sigmar, *Phys. Plasmas* **3**:293 (1996).
20. G. Vahala, L. Vahala, and J. Morrison, *Phys. Plasmas* **4**:3992 (1997).
21. X. He and L. Luo, *Phys. Rev. E* **55**:R6333 (1997).